

# Sparse Object-level Supervision for Instance Segmentation with Pixel Embeddings

Adrian Wolny   Qin Yu   Constantin Pape   Anna Kreshuk\*

European Molecular Biology Laboratory  
Heidelberg, Germany

## Abstract

Most state-of-the-art instance segmentation methods have to be trained on densely annotated images. While difficult in general, this requirement is especially daunting for biomedical images, where domain expertise is often required for annotation. We propose to address the dense annotation bottleneck by introducing a proposal-free segmentation approach based on non-spatial embeddings, which exploits the structure of the learned embedding space to extract individual instances in a differentiable way. The segmentation loss can then be applied directly on the instances and the overall method can be trained on ground truth images where only a few objects are annotated, from scratch or in a semi-supervised transfer learning setting. In addition to the segmentation loss, our setup allows to apply self-supervised consistency losses on the unlabeled parts of the training data. We evaluate the proposed method on challenging 2D and 3D segmentation problems in different microscopy modalities as well as on the popular CVPPP instance segmentation benchmark where we achieve state-of-the-art results.

The code is available at: <https://github.com/kreshuklab/spoco>.

## 1. Introduction

Instance segmentation is one of the key problems addressed by computer vision. It is important for many application domains, from astronomy to scene understanding in robotics, forming the basis for the analysis of individual object appearance. Biological imaging provides a particularly large set of use cases for the instance segmentation task, with imaging modalities ranging from natural photographs for phenotyping to electron microscopy for detailed analysis of cellular ultrastructure. The segmentation task is often posed in crowded 3D environments or their 2D projections

with multiple overlapping objects. Additional challenges – compared to segmentation in natural images – come from the lack of training data which has to be annotated by experts, as well as from the high requirements to segmentation accuracy posed by downstream analysis tasks.

Over the recent years, the introduction of spatial and non-spatial pixel embedding networks has allowed for substantial progress on the crowded environment problem [40, 22, 27, 3, 7, 34], but the remaining prerequisite of providing densely segmented images for training continues to stifle the adoption of the state-of-the-art methods in everyday image analysis practice. Several existing approaches to weak supervision for instance segmentation relax the object mask annotations to bounding boxes [25, 29, 42, 35], but still require every object to be annotated. Similarly, semi-supervised instance segmentation methods [6, 5, 9] propagate labels into the unlabeled areas, but cannot selectively exploit sparse object annotations. Self-supervised approaches have recently been extended to the semantic segmentation task [16], but their powerful consistency constraints have so far not been applied on the single instance level.

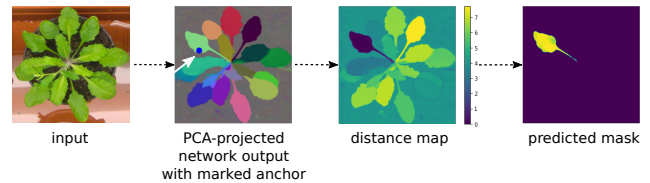


Figure 1. Differentiable instance selection for non-spatial embedding networks. First, we sample an anchor point on the instance, randomly or guided by the groundtruth instances (see Algorithm 1). An example anchor on one of the leaves is highlighted by the white arrow in the (column 2). Second, we compute a distance map in the embedding space from the anchor point to all image pixels (column 3). In the final step, we apply soft thresholding (Equation 4), which transforms the distance map to the instance mask (column 4).

\*Correspondence to: [anna.kreshuk@embl.de](mailto:anna.kreshuk@embl.de)

The aim of our contribution is to address the dense annotation bottleneck by introducing a differentiable step which allows for any (differentiable) *instance-level* loss function in the training of a non-spatial pixel embedding network (Figure 1). We show that even with dense annotations and thus full supervision, application of the loss at the single instance level consistently improves the performance across a variety of datasets. To extend the setup to sparsely annotated training data, we introduce additional terms in the discriminative loss [7] which enable us to train the embedding network in a "positive unlabeled" setting, i.e. with no labels in the background class and only a few labeled instances. Furthermore, the instance selection step can be applied to the unlabeled areas of the training images, enabling integration of sparse object supervision with the recently introduced unsupervised visual representation learning methods [20, 10]. Here, we add a second slowly changing embedding network and an additional loss term to maintain embedding consistency of the instances and the background in the unlabeled regions. This term brings a further improvement of the network predictions at all supervision levels, in direct prediction and in the transfer learning setting.

In summary, we address the instance segmentation task with non-spatial embeddings and (1) propose a way to select individual instances directly in training (Figure 1), (2) propose an extension to the regular discriminative loss [7] of embedding networks which can be applied to images where only some of the objects and none of the background are labeled, (3) add a consistency loss term that allows for instance-level training on unlabeled image regions, (4) reach state-of-the-art results on the popular CVPPP instance segmentation benchmark and show on challenging microscopy datasets that the bulk of network performance improvement happens after a fraction of training objects are annotated.

## 2. Related work

Proposal-based methods such as Mask R-CNN [21] are a popular choice for instance segmentation in natural images. These methods can be trained from weak bounding box labels [25, 29, 42, 35]. However, as they require a pre-trained backbone network and have difficulties segmenting complex non-convex shapes, they have not become the go-to segmentation technique for microscopy imaging.

Traditionally, instance segmentation methods for microscopy started from the semantic segmentation task, with either objects [39] or object boundaries [4, 15, 28] serving as the foreground class. Instances were then recovered by post-processing with connected components labeling, watershed transform or graph-based agglomeration [4, 15, 28, 36]. Recently, methods based on learned pixel embeddings started to gain a lot of popularity [40, 22, 27, 3]. Their main advantage lies in their superior performance for

overlapping objects and crowded environments as well as in the general simplification of the pipeline: the same method can now be trained for intensity-based and for boundary-based segmentation.

Semantic instance segmentation with embedding networks was introduced by [7]. These networks learn how to place the pixels of the input image into a high-dimensional vector space in which the pixels from the same instance form a tight cluster away from other pixels. The embeddings of [7] have no explicit spatial or semantic component. Spatial awareness can be introduced by passing pixel coordinates to the network [30] or by explicitly predicting foreground areas and, for pixels in those, the direction to the object center [34, 11], the distance to the object boundary [40, 2] or the shape of the objects in the local patch [22, 3]. Overall, spatial embeddings have substantially improved the performance of embedding-based segmentation algorithms, delivering state-of-the-art results in many benchmarks, including those for biological data [22].

However, just like the original proposal of [7], all modern embedding networks require fully segmented images for training and compute the loss for the whole image rather than for individual instances. Here, an interesting proposal has been made by [34]: the clustering bandwidth is learned in the network training which allows to optimize the intersection-over-union loss for each instance. Still, as the network also needs to be trained to predict a seed map of cluster centers for inference, this method cannot be trained on partially labeled images either. Differentiable single instance selection has also been proposed by AdaptIS [41]. However, this method does not use a learned pixel embedding space and thus requires an additional sub-network to perform instance selection and cannot be combined with the discriminative loss of [7]. It also relies on a pre-trained backbone network, which is rarely available for microscopy images. Importantly, AdaptIS does not introduce training from sparse "positive unlabeled" annotations.

Self-supervised methods acting without any training data are proving to be very successful for image classification and, since very recently, semantic segmentation tasks [16]. These methods heavily exploit network consistency conditions [20, 10, 18]. However, they have so far not been applied in a semi-supervised *instance* segmentation setting, especially not in a regime where no labels for background are present. Similarly to the object-wise segmentation losses, the major difficulty in extending the network prediction consistency loss to the instance segmentation task lies in the lack of a method to select individual instances in a differentiable way during training.

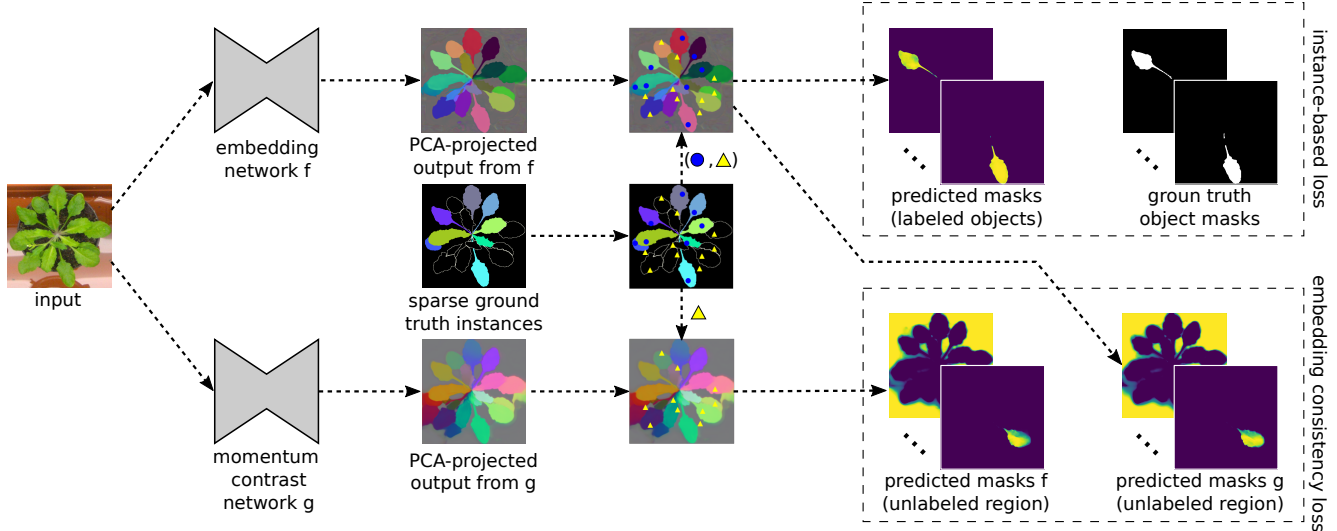


Figure 2. Overview of the proposed training procedure. An embedding network  $f$  is trained with the Sparse Single Object loss (section 3.2). An input image is passed through two embedding networks  $f(\cdot)$  and  $g(\cdot)$  resulting in two vector fields  $\mathcal{E}_f$  and  $\mathcal{E}_g$ . Anchor pixels inside labeled objects (blue dots) are sampled and their corresponding instances are extracted as shown in Fig. 1. Discrepancy between extracted objects and ground truth objects is minimized by the instance-based loss  $L_{obj}$  (Eq. 5). Another set of anchors (yellow triangles) is sampled exhaustively from the unlabeled region and for each anchor two instances are selected based on  $\mathcal{E}_f$  and  $\mathcal{E}_g$  embeddings. Minimization of the discrepancy between the two instances using  $L_{U.con}$  loss (Eq. 8) aims to improve consistency between  $\mathcal{E}_f$  and  $\mathcal{E}_g$  in the unlabeled regions.

### 3. Methods

#### 3.1. Single Object loss

First, recall that the discriminative loss of [7] consists of a variance, a distance and a regularization term:

$$L_{var} = \frac{1}{C} \sum_{k=1}^C \frac{1}{N_k} \sum_{i=1}^{N_k} [\|\mu_k - e_i\| - \delta_v]_+^2 \quad (1)$$

$$L_{dist} = \frac{1}{C} \sum_{k_a=1}^C \sum_{k_b=1}^C [2\delta_d - \|\mu_{k_a} - \mu_{k_b}\|]_+^2 \quad (2)$$

$$L_{reg} = \frac{1}{C} \sum_{k=1}^C \|\mu_k\| \quad (3)$$

It works by pulling and pushing the image pixels into spheres in a high-dimensional embedding space  $\mathcal{E} = \{e_0, e_1, \dots, e_N\}$ , where  $N = \sum_{k=1}^C N_k$  is the number of pixels in the image,  $N_k$  is the number of pixels belonging to object  $I_k$  and  $C$  is the number of objects, including background. The pull force  $L_{var}$  brings the instance pixels closer to their mean embedding  $\mu_k$ , while the push force  $L_{dist}$  separates the embedding spheres of different instances. We exploit the clustering induced by this loss to select pixels belonging to a single instance and apply auxiliary losses at the instance level (Figure 2). Crucially, we find that given a set of instances  $\mathcal{I} = \{I_0, I_1, \dots, I_C\}$  it

is possible to extract a 'soft' mask  $S_k$  for the current network prediction of a given instance  $I_k$  in a *differentiable* way (Figure 1). We select an anchor point for  $I_k$  and project it into the learned embedding space  $\mathcal{E}$  to recover its embedding  $A_k$ , which we term anchor embedding. We compute the distance map from all image pixel embeddings to the anchor embedding ( $\|e_i - A_k\|$ ) and apply a Gaussian kernel function  $\phi$  to "softly" select the pixels within the given radius  $\delta_v$  (the margin from the variance term from Equation 1)

$$S_k = \{s_k \mid s_k = \phi(e_i)\} \quad (4)$$

$$\phi(e_i) = \exp\left(-\frac{\|e_i - A_k\|^2}{2\sigma^2}\right).$$

The embeddings within the distance  $\delta_v$  from the anchor embedding  $A_k$  should have a kernel value greater than a predefined threshold  $t$ , i.e.  $\phi(e_i) > t \iff \|e_i - A_k\| < \delta_v$ . Choosing  $t = 0.5$ , we can thus determine  $\sigma$ : Given  $\exp\left(-\frac{\delta_v^2}{2\sigma^2}\right) = 0.5$ , we get  $\sigma = \frac{\delta_v}{\ln 0.5}$ .

We can now formulate a loss for a single object segmentation mask by maximizing the Dice score ( $D$ ) [32] of the mask  $S_k$  predicted using Equation 4 and the corresponding ground-truth mask  $I_k$ .

$$L_{obj} = \frac{1}{C} \sum_{k=1}^C 1 - D(S_k, I_k) \quad (5)$$

When sampling anchor points for  $I_k$  we select a random pixel whose embedding is within the  $\delta_v$ -radius of the mean

instance embedding at every iteration. The anchor selection procedure is described in Algorithm 1. The effectiveness of the using random anchor points is comparable to always choosing the mean instance embedding (see ablation study in Appendix A.2) and it helps preserving true positive instances when consistency clustering is used for inference (Algorithm 2).

Combining the losses in Eq. 1, Eq. 2, Eq 3 and Eq. 4, we obtain:

$$L_{SO} = \alpha L_{dist} + \beta L_{var} + \gamma L_{reg} + \lambda L_{obj} \quad (6)$$

which we refer to as the Single Object contrastive loss ( $L_{SO}$ ). In our experiments we use  $\alpha = \beta = \lambda = 1$  and  $\gamma = 0.001$ .

---

#### Algorithm 1: Anchor Sampling

---

**Input:** Set of instances  $\mathcal{I}$ , distance  $\delta_v$

**Output:** Set of anchors  $\mathcal{A}$

$\mathcal{A} = \{\};$

**for**  $I_k \in \mathcal{I}$  **do**

$A_k = \text{null};$

$\mu_k = \text{mean embedding of } I_k;$

    //  $\tau$  is a random permutation

**for**  $e_i \in \tau(I_k)$  **do**

**if**  $\|\mu_k - e_i\| < \delta_v$  **then**

$A_k = e_i;$

**if**  $A_k$  is null **then**

$A_k = \mu_k;$

$\mathcal{A} = \mathcal{A} \cup \{A_k\};$

**return**  $\mathcal{A};$

---

### 3.2. Sparse Single Object loss

To enable training from images, where only some of the objects are labeled and no labels are present in the background, we introduce two additional loss terms: one which pushes each cluster away from the pixels in the unlabeled region and the other which enforces embedding space consistency in the unlabeled region. Given the unlabeled region  $U$  which can contain both background and unlabeled instances, we define an additional "push" term:

$$L_{U\_dist} = \frac{1}{C} \sum_{k=1}^C \frac{1}{N_U} \sum_{i=1}^{N_U} [\delta_d - \|\mu_k - e_i\|]_+^2 \quad (7)$$

where  $C$  is the number of labeled clusters/instances and  $N_U$  is the number of pixels in the unlabeled region  $U$ .

Since there is no direct supervision applied onto the unlabeled part of the image, the embedding network is free to overfit on the high frequency patterns present in there.

This is true especially for natural images and microscopy images with complex background structures, e.g. electron microscopy (see Figure 3). To overcome this issue we introduce the embedding consistency term (Figure 2). Having two different embedding networks  $f$  and  $g$ , we augment a given input image  $x$  with two different augmentation operators  $t$  and  $t'$  (data augmentations must preserve objects location and geometry, e.g. noise and color distortions) and pass it through  $f$  and  $g$  respectively. The resulting two vector fields  $\mathcal{E}_f = f(t(x))$  and  $\mathcal{E}_g = g(t'(x))$  come from the same input geometry, hence we would like them to result in consistent instance segmentation after clustering, also in the unlabeled part of the input. To enforce this consistency we randomly sample an anchor point from the unlabeled region, project it into the two embedding spaces  $\mathcal{E}_f, \mathcal{E}_g$ , to get anchor embeddings  $A^f$  and  $A^g$  and compute two "soft" masks  $S^f$  and  $S^g$  according to Equation 4. Similarly to Equation 5 the embedding consistency loss is given by maximising the overlap of the two masks, using the Dice coefficient ( $D$ ):

$$L_{U\_con} = \frac{1}{K} \sum_{k=1}^K 1 - D(S_k^f, S_k^g) \quad (8)$$

where  $K$  is the number of anchor points sampled from the unlabeled region  $U$  such that the whole region is covered by the union of extracted masks, i.e.  $U \approx \bigcup_{k=1}^K S_k^f \cup S_k^g$ . For the sake of computation efficiency we choose a MoCo-based scheme [20] where  $g$  is implemented as a momentum-based moving average of the embedding network  $f$  and only the parameters  $f$  are updated by back-propagation (implementation details in Appendix A.1). Importance of the embedding consistency term is illustrated in Figure 3. Note how the complex patterns present in the background (e.g. the pot) are propagated into the embedding space of the network trained without the consistency term, leading to spurious objects in the background after clustering. In contrast, the same network trained with the embedding consistency loss produces a much more uniform vector field in the background with no false positives. Both networks were trained using only 10% of ground truth objects. Visually the homogeneity of the background for embeddings of the network trained sparsely with the consistency term is similar to the one produced by the network trained with full supervision and  $L_{SO}$  loss shown (Fig. 3right). Apart from images with structured background, the embedding consistency term is crucial when a small number ( $< 10\%$ ) of ground truth object is provided, where it acts as a strong regularizer, reducing overall overfitting.

Our final loss, termed Sparse Single Object loss ( $L_{SSO}$  is a linear combination of the Single Object loss  $\hat{L}_{SO}$  applied to the labeled object and the two additional terms  $L_{U\_dist}$  and  $L_{U\_con}$  associated with the unlabeled region:

$$L_{SSO} = \hat{L}_{SO} + \delta \cdot L_{U.dist} + \epsilon \cdot L_{U.con} \quad (9)$$

In our experiments we use  $\delta = \epsilon = 1$ .

Figure 2 gives a graphical overview of our training procedure. We name our method *SPOCO* (SParse Object Consistency Loss). In experiments we use the term SPOCO to refer to the fully supervised training (taking all ground truth objects including the background object). SPOCO@p refers to the semi-supervised setting, in which a fraction  $p \in (0, 1]$  of objects (excluding background) is taken for training. The background label is never selected in the semi-supervised setting, i.e. SPOCO@1.0 means that the network was trained with all labeled objects, excluding background.

### 3.3. Inference

After training, we obtain the final instance segmentation by applying a clustering algorithm to the predicted embeddings. Mean-shift [13] and HDBSCAN [8] are commonly used for this task [7, 27, 37]. For our use case of sparse object training, mean-shift has a high recall and low precision since it tends to over-segment the image in structured background region resulting in high number of false positives. In contrast, density-based clustering considers areas of low density to only contain noise and thus recovers much better segmentations for images with highly structured background. The downside of HDBSCAN is its sensitivity to the *min\_size* hyperparameter. In this work we experimented with two clustering schemes: (1) HDBSCAN and (2) a hybrid approach called *consistency clustering*. Briefly, an input image is augmented with two different test time transformations and their embeddings  $\mathcal{E}_f$  and  $\mathcal{E}_g$  are predicted by networks  $f$  and  $g$  (momentum contrast) respectively. We cluster  $\mathcal{E}_f$  using mean-shift with bandwidth set to the pull force margin  $\delta_v$ . Then for each segmented object  $S_k$ , we randomly select  $M$  anchor points and for each anchor we extract a new object  $\hat{S}_k^m$  by taking a  $\delta_v$ -neighborhood around the anchor in the  $\mathcal{E}_g$  space. If the median intersection-over-union (IoU) between  $S_k$  and each of the  $\hat{S}_k^m$  objects is lower than a predefined threshold, we discard  $S_k$  from the final segmentation (see Algorithm 2). This is based on the premise that clusters corresponding to the real objects should remain consistent between  $\mathcal{E}_f$  and  $\mathcal{E}_g$  (see Appendix A.3 for a comparison of different clustering schemes).

### 3.4. Other single-instance losses

Our approach allows for any differentiable loss function at the single instance level. In addition to the Dice loss (Eq. 5), we evaluated an adversarial training approach. Our pixel embedding network served as a generator of object masks, which the discriminator of the Wasserstein GAN [1]

---

#### Algorithm 2: Consistency clustering

---

**Input:** Set of segmented objects  $\mathcal{S}$ , output from momentum contrast network  $\mathcal{E}_g$ , IoU threshold  $t_{IoU}$

**Output:** New set of segmented objects  $\hat{\mathcal{S}}$

```

 $\hat{\mathcal{S}} = \{\};$ 
for  $S_k \in \mathcal{S}$  do
   $\mathcal{A}_k = \{A_k^1, \dots, A_k^M \mid A_k^m \in \mathcal{E}_g\}$  - anchors of  $S_k$ ;
   $I_{IoU} = \{\};$ 
  for  $A_k^m \in \mathcal{A}_k$  do
     $\hat{S}_k^m = \{s_i \mid s_i = \|e_i^g - A_k^m\| < \delta_v\}$ ;
     $I_{IoU} \cup \text{IoU}(\hat{S}_k^m, S_k)$ ;
  if  $\text{med}(I_{IoU}) > t_{IoU}$  then
     $\hat{\mathcal{S}} = \hat{\mathcal{S}} \cup \{S_k\}$ ;
return  $\hat{\mathcal{S}}$ ;

```

---

learned to distinguish from the ground truth object segmentation masks. The generator loss was computed as:

$$\alpha L_{dist} + \beta L_{var} + \gamma L_{reg} + \lambda L_{wgan} \quad (10)$$

In our experiments, adversarial training does not by itself bring a larger performance improvement than the Dice-based loss. Both losses can also be used in combination which can be very beneficial: as we show in Table 3, the combined loss outperforms a much more complex 3-step state-of-the-art segmentation pipeline. This finding is similar to [31] where authors use an adversarial approach to train a semantic segmentation model. Our approach differs, as in our setup the discriminator focuses more on the individual object properties instead of the global statistics of the semantic mask predicted by the network.

We refer to Appendix A.1 for a detailed training setup, architecture and hyperparameter selection for the adversarial training case.

## 4. Experiments

### 4.1. Datasets

**CVPPP dataset.** We used the A1 subset of the popular CVPPP dataset [33] which is part of the LSC competition. The task is to segment individual leaf instances of a plant growing in a pot. The dataset consists of 128 training images with public ground truth labels and 33 test images with no publicly available labels. Test images come with a foreground mask which can be used during inference.

**DSB2018 dataset.** From a collection of 670 manually annotated images of cell nuclei from the 2018 Data Science Bowl challenge [24], we randomly select 536 images for training, 67 for validation and 67 for testing.

**Light microscopy datasets.** To evaluate the performance of our approach on a challenging boundary-based

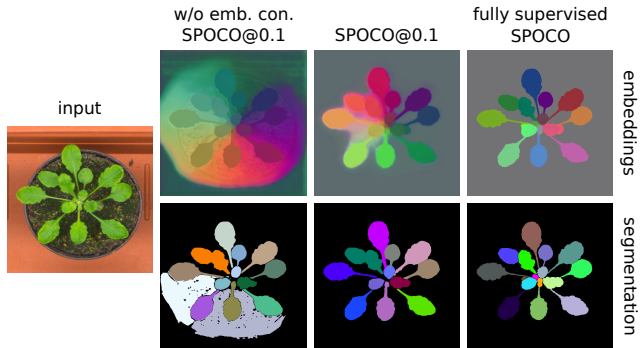


Figure 3. Qualitative comparison of the embeddings produced by the networks trained with two variants of the SPOCO@0.1 (10% of the ground truth objects): (column 2) without and (column 3) with the embedding consistency term. 16d pixel embeddings have been PCA projected into the RGB space for visualization. Column 1: a sample image from the CVPPP test set. Column 4 shows embeddings which arise from SPOCO trained with full supervision (including the background label). HDBSCAN clustering ( $min\_size = 200$ ) results are shown in row 2. Spurious background clusters arise from the embeddings trained without the consistency term.

segmentation task we selected a 3D light microscopy dataset of the ovules of *Arabidopsis thaliana* from [45]. There are 48 image stacks in total: 39 for training, 2 for validation and 7 for testing. Additionally we use the 3D *Arabidopsis thaliana* apical stem cells from [44] in a transfer learning setting. The images are from the same imaging modality as the ovules dataset (confocal, cell membrane stained), but differ in cell type and image acquisition settings. We choose the Ovules dataset as the source domain and Stem cells as the target (*plant1*, *plant2*, *plant4*, *plant13*, *plant15* are used for fine-tuning and *plant18* for testing).

**Electron Microscopy (EM) datasets.** Here we test our method in the transfer learning setting on the problem of mitochondria segmentation in EM data. An important difference between light and electron microscopy from the segmentation perspective lies in the appearance of the background which is simply dark and noisy for light microscopy and highly structured for EM. The source domain (VNC dataset) [17] is a small annotated  $20 \times 1024 \times 1024$  volume of the *Drosophila larva* ventral nerve cord acquired with serial section Transmission Electron Microscopy (ssTEM) with voxel size of  $50 \times 5 \times 5$  nm. We use 13 consecutive slices for training and keep 7 slices for validation. As target domain we choose the 3D MitoEM-R dataset from the MitoEM Challenge [43] a  $500 \times 4096 \times 4096$  volume at  $30 \times 8 \times 8$  nm resolution extracted from rat cortex with Serial Blockface Electron Microscopy (SBEM). Slices (0-399) are used for fine-tuning and (400-499) for testing.

## 4.2. Setups

Unless stated otherwise in all our experiments we used a 16 dimensional embedding space, pull margin  $\delta_v = 0.5$  and push margin  $\delta_d = 2.0$ . Any fully convolutional architecture producing dense outputs could be used for the embedding network, we choose the U-net [39] as the de facto standard in microscopy image segmentation, with its 3D variant [12] used for the volumetric dataset. We use the Adam [26] optimizer with initial learning rate of  $lr = 0.0002$  and data augmentation transforms consisting of random crops, random flips, random rotations, random scaling and elastic deformations. For the momentum contrast embedding network, we additionally use additive Gaussian noise, Gaussian blur and color jitter as geometry preserving transformations. The depth of the U-Net is chosen such that the receptive field of features in the bottleneck layer is equal to the input patch size.

In transfer learning experiments the source network is always trained with the full ground truth. For fine-tuning we reduce the learning rate by a factor of 10 compared to the source network and use only a small fraction of the objects from the target. The VNC dataset is too small to train a 3D U-net, so we perform the segmentation in 2D, slice by slice. We also downsample the VNC dataset by factor 1.6 in XY to match the voxel size of the target MitoEM data.

Please refer to the Appendix A.1 for a detailed description of the network architectures, training procedure and hyperparameter selection.

## 4.3. Results and Discussion

**CVPPP dataset.** The challenge measures the count of segmented objects ( $|DiC|$ ) and their segmentation accuracy as Symmetric Best Dice (SBD) score (Table 1). The challenge provides a foreground mask which can be used in inference, we assume it has been used by authors of [7, 38, 27]. In this setting, SPOCO outperforms Harmonic Embeddings and the current winner of the leaderboard on the A1 dataset, keeping the advantage even in the case when the foreground mask is not given, but learned by another network (“predicted FG”). Even without using the foreground mask in the final clustering, SPOCO is close to Harmonic Embeddings in segmentation accuracy, achieving much better average difference in counting score ( $|DiC|$ ). We evaluate semi-supervised predictions without using the foreground mask as we cannot easily train a semantic network without background labels. Nevertheless, even when training with only 10% of the ground truth leaf instances (SPOCO@0.1), the SBD as compared with the fully supervised SPOCO (without FG) drops only by 10 percent points. Qualitative results from SPOCO@0.1 can be seen in Figure 3 (column 3), where the single under-segmentation error is present in the top left part of the image. The embedding consistency term substantially improves SPOCO

Method	SBD	$ DiC $
Discriminative loss [7]	0.842	1.0
Recurrent attention [38]	0.849	<b>0.8</b>
Harmonic Emb. [27]	0.899	3.0
SPOCO (GT FG)	<b>0.932</b>	1.7
SPOCO (pred FG)	0.920	1.6
SPOCO (w/o FG)	0.886	1.3
@0.1	$0.788 \pm 0.017$	$5.4 \pm 0.3$
@0.1 w/o $L_{U\_con}$	$0.720 \pm 0.037$	$6.3 \pm 0.1$
@0.4	$0.824 \pm 0.003$	$3.2 \pm 0.5$
@0.4 w/o $L_{U\_con}$	$0.738 \pm 0.019$	$2.1 \pm 0.1$
@0.8	$0.828 \pm 0.010$	$1.6 \pm 0.2$
@0.8 w/o $L_{U\_con}$	$0.810 \pm 0.010$	$2.1 \pm 0.2$

Table 1. Results on the test set of the CVPPP leaf segmentation challenge. The scores for fully supervised SPOCO are reported in 3 different clustering settings: (1) with the ground truth foreground mask, (2) with the foreground mask predicted by a separately trained U-Net, (3) without the foreground mask. Results for semi-supervised setting SPOCO@p (without foreground mask) are presented for 10%, 40% and 80% of randomly selected ground truth instances with and without the embedding consistency term.

Method	AP@0.5	mAP
U-Net baseline	0.642	0.463
StarDist [40]	0.764	0.533
Discriminative loss (predicted FG)	0.767	0.569
SPOCO (predicted FG)	<b>0.779</b>	<b>0.576</b>

Table 2. Segmentation results on the test set of DSB2018 nuclei segmentation challenge.

performance with sparse training data. HDBSCAN with  $min\_size = 200$  was used for clustering everywhere.

**DSB2018 dataset.** Here we compare SPOCO with the simple U-Net baseline, with the popular StarDist [40] model - a strong baseline for segmenting star-convex cells, and with an embedding network trained with standard discriminative loss [7]. The U-Net baseline predicts a foreground probability map, thresholded at the value of 0.5 and segmented with the connected components algorithm. SPOCO achieves the best mean average precision on the test set when clustered with HDBSCAN ( $min\_size = 40$ ) over the foreground mask predicted by the U-Net baseline.

**3D light microscopy datasets.** We compare SPOCO to the method of [45]: a 3-step pipeline of boundary prediction, supervoxel generation and graph agglomeration. Following [45], adapted Rand error (ARand error) [14] is used for evaluating the segmentation accuracy. As shown in Table 3, the performance of SPOCO is close to that of the much more complex 3-step PlantSeg pipeline. An additional adversarial loss term (SPOCO with  $L_{WGAN}$ ) brings another performance boost and improves SPOCO accuracy beyond the PlantSeg level.

Method	ARand error
PlantSeg [45]	0.046
Discriminative loss [7]	0.074
SPOCO	0.048
SPOCO with $L_{WGAN}$	<b>0.042</b>
SPOCO@0.1	0.069
SPOCO@0.4	0.060
SPOCO@0.8	0.057

Table 3. Evaluation on a 3D light microscopy dataset of Arabidopsis Ovules [45]. The Adapted Rand error (ARand error) averaged over the 7 test set 3D stacks is reported. Bottom part of the table shows the scores achieved in the sparse object setting, where 10%, 40% and 80% of ground truth instances are used for training respectively.

Method	ARand error
Stem only	0.074
Ovules only	0.227
Ovules+Stem@0.01	$0.141 \pm 0.002$
Ovules+Stem@0.05	$0.109 \pm 0.002$
Ovules+Stem@0.1	$0.106 \pm 0.004$
Ovules+Stem@0.4	$0.093 \pm 0.003$
Ovules+Stem@0.8	$0.090 \pm 0.003$

Table 4. Evaluation on a 3D light microscopy dataset in a transfer learning setting. Ovules dataset acts as the source domain, Stem dataset as target. Performance is shown as adapted Rand error, lower is better. Mean  $\pm$  SD are reported across 3 random samplings of the instances from the target dataset.

Note that SPOCO trained with 10% of the groundtruth instances already outperforms the original embedding network with discriminative loss [7]. See Figure 4 (top row) for qualitative results on a randomly sampled test set patch.

Table 4 shows SPOCO performance in a transfer learning setting, when finetuning a network trained on the Ovules dataset to segment the Stem dataset. The Ovules network trained only on source data did not perform very well, but just 5% of the target groundtruth annotations brought a two-fold improvement in segmentation accuracy. Results in tables 3 and 4 were computed with HDBSCAN ( $min\_size = 550$ ).

Qualitative results are shown in Figure 4 (bottom row). Note how the output embeddings from the Ovules network fine-tuned with just 1% of cells from the target dataset are less crisp due to the domain gap, but the clustering is still able to segment them correctly.

**Electron Microscopy datasets.** Table 5 continues the evaluation of SPOCO performance in a transfer learning setting. We report the average precision for different IoU threshold 0.5 (AP@0.5) and the mean average precision (mAP) between the predicted and ground truth objects. Similar to the light microscopy case, just 1% of annotated

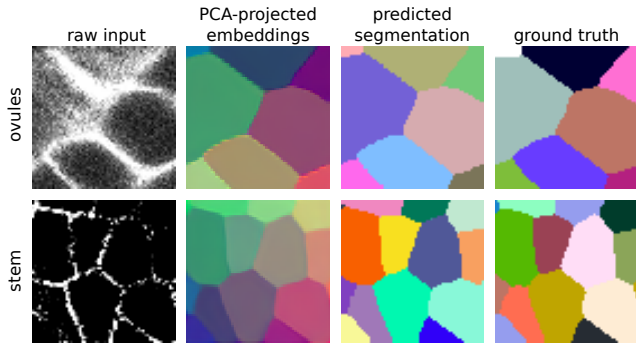


Figure 4. Qualitative results for light microscopy segmentation in standard and transfer learning settings. (Top) Segmentation of a random 3D patch from the test set Ovules dataset. (Bottom) Output of the source network fine-tuned with 1% of instances from the Stem (column 2) and corresponding segmentation (column 3).

objects in the target dataset bring a 1.5 fold improvement in the mean average precision compared to the network trained on source VNC domain only. A comparison to a network trained on MitoEM from scratch (Table 5 bottom) shows that fine-tuning does significantly improve performance for low amounts of training data (1% of the target). The qualitative results in Figure 5 show the segmented outputs from the VNC net, the version fine-tuned with 5 % of labels, with (MitoEM@0.05) and without (MitoEm@0.05 w/o emb. con.) consistently loss as well as the network trained fully on the target domain (MitoEM net). The VNC net only partially recovers 4 out of 7 ground-truth instances and also produces a false positive. MitoEM@0.05 without consistency loss only recovers 2 instances, while the version with consistency loss and MitoEM net recover the correct segmentation. HDBSCAN with  $min\_size = 600$  was used for clustering.

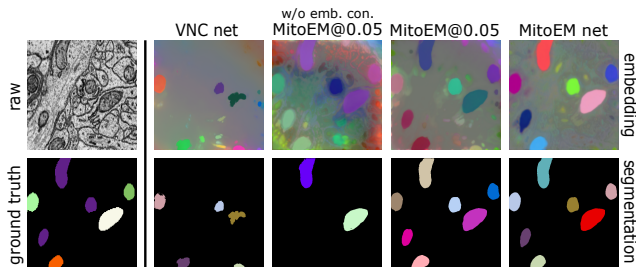


Figure 5. Qualitative results for 2D electron microscopy segmentation in the transfer learning setting. Top row shows the raw data and the RGB-projected outputs from the following 4 networks from left to right: VNC from scratch, VNC+MitoE@M0.05 without embedding consistency loss term, VNC+MitoEM@0.05 with embedding consistency loss term, MitoEM from scratch. Bottom row: ground truth and predicted segmentation.

Method	AP@0.5	mAP
VNC	0.234	0.137
VNC-MitoEM		
@0.01	$0.368 \pm 0.022$	$0.247 \pm 0.022$
@0.01 w/o $LU_{con}$	$0.306 \pm 0.014$	$0.210 \pm 0.008$
@0.05	$0.398 \pm 0.007$	$0.277 \pm 0.006$
@0.05 w/o $LU_{con}$	$0.319 \pm 0.002$	$0.227 \pm 0.002$
@0.10	$0.389 \pm 0.013$	$0.268 \pm 0.007$
@0.10 w/o $LU_{con}$	$0.301 \pm 0.012$	$0.212 \pm 0.007$
MitoEM		
@0.01	$0.088 \pm 0.045$	$0.046 \pm 0.025$
@0.05	$0.403 \pm 0.055$	$0.280 \pm 0.046$
@0.10	$0.481 \pm 0.008$	$0.340 \pm 0.007$
Full supervision	0.560	0.429

Table 5. Evaluation on a MitoEM dataset (target) fine-tuned from the VNC net (upper part) and trained from scratch (lower part). The performance is measured through average precision (AP@0.5, mAP). Mean  $\pm$  SD are reported across 3 random samplings of the instances from the target dataset. We show the scores without the embedding consistency term in the unlabeled regions (w/o  $LU_{con}$ ) for comparison.

## 5. Conclusion

We presented a new approach to training a pixel embedding network which allows to apply the loss to individual objects, without any additional spatial component such as "seediness" or "objectness" score. We demonstrate its competitiveness on the popular CVPPP instance segmentation benchmark as well as on two microscopy datasets with intensity- and boundary-based segmentation problems.

We further expand the advantages of such per-object training by extending the discriminative loss to enable training from images where only some of the objects and none of the background are annotated. Such sparse training regime is especially important for biological data where pixel-level annotations are usually very expensive to obtain. We compensate for the lack of the background labels and general label sparsity by another loss term enforcing network prediction consistency through a MoCo-like setup [20] on the instance level. We evaluate the sparse supervision approach on data from light and electron microscopy, in 2D and 3D, in direct prediction and in transfer learning. In all cases, the network demonstrates strong segmentation performance at a very reduced manual annotation cost.

In the future, we plan to further explore different single-object losses, building on our promising adversarial learning experiments. Other interesting directions include addition of a semantic branch and general extension to panoptic segmentation as well as further reduction of the necessary amount of expensive manual annotations through more extensive self-supervised pre-training.



## A. Appendix

### A.1. Network architectures and training parameters

The structure of the U-Net embedding network used for each dataset is described using the building block shown in Figure 6. The number of ConvBlocks in the encoder/decoder part of U-Net is chosen such that the receptive field of features in the last encoder layer is equal to or slightly bigger than the input size. We used group normalization [46] for 3D and electron microscopy experiments and batch normalization for CVPPP and DSB2018 datasets [23].

In the tables describing the architecture: second number after the comma corresponds the number of output channels from each layer, *Upsample* denotes nearest-neighbor upsampling and *Concat* denotes channel-wise concatenation of the output for a given decoder layer with the output from the corresponding encoder layer.

Unless otherwise specified, Adam optimizer [26] with an initial learning rate of 0.0002, weight decay  $10^{-5}$ ,  $\beta_1 = 0.9$  and  $\beta_2 = 0.999$  was used for training. Learning rate was reduced by a factor of 0.2 when the validation loss stopped improving after a dataset-dependent number of iterations. Training was stopped when the learning rate dropped below  $10^{-6}$  or maximum number of iterations was reached. In all our experiments we use 16-dimensional embedding space, i.e. the output from the U-Net after the last  $1 \times 1$  convolution has 16 channels. Input images were globally normalized to zero mean and a standard deviation of one unless stated otherwise.

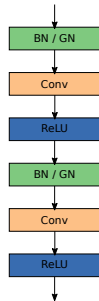


Figure 6. ConvBlock architecture. We use *ConvBlock*, *ConvBlockBN* or *ConvBlockGN* to refer to the block where *no*, *batch* or *group* normalization is used respectively.

**CVPPP dataset.** Table 6 shows the 2D U-Net architecture used in the experiment. All networks were trained for up to 80K iterations (unless the stopping criteria was not satisfied before) with a minibatch size of 4. Input images were randomly scaled, flipped horizontally and vertically and cropped to  $448 \times 448$  pixels. Before passing to  $f(\cdot)$  and  $g(\cdot)$  networks, random color jitter and Gaussian blur were

applied.

3-channel image $x \in \mathbb{R}^{M \times M \times 3}$
ConvBlockBN, 16, MaxPool $2 \times 2$
ConvBlockBN, 32, MaxPool $2 \times 2$
ConvBlockBN, 64, MaxPool $2 \times 2$
ConvBlockBN, 128, MaxPool $2 \times 2$
ConvBlockBN, 256, MaxPool $2 \times 2$
ConvBlockBN, 512, Upsample $2 \times 2$
Concat, 256 + 512
ConvBlockBN, 256, Upsample $2 \times 2$
Concat, 128 + 256
ConvBlockBN, 128, Upsample $2 \times 2$
Concat, 64 + 128
ConvBlockBN, 64, Upsample $2 \times 2$
Concat, 32 + 64
ConvBlockBN, 32, Upsample $2 \times 2$
Concat, 16 + 32
ConvBlockBN, 16, conv $1 \times 1$ , $d = 16$

Table 6. U-Net architecture for CVPPP and DSB2018 datasets.  $M = 448$  for CVPPP and  $M = 256$  for DSB2018.

**DSB2018 dataset.** See Table 6 for an overview of 2D U-Net architecture for the DSB2018 cell segmentation. All networks were trained for up to 100K iterations with a minibatch size of 4. Input images were randomly cropped to  $256 \times 256$  patches, randomly rotated and flipped. Before passing to  $f(\cdot)$  and  $g(\cdot)$  networks, Gaussian noise with randomly selected  $\sigma$  was added to the input. Percentile normalization  $(x - p_{min}) / (p_{max} - p_{min})$  was applied to the input, where  $p_{min}$ ,  $p_{max}$  are the 1-percentile and 99.8-percentile of the raw intensities respectively.

**Light microscopy datasets.** 3D U-Net architecture used for the light microscopy datasets is shown in Table 7. Ovules networks were trained for up to 200K iterations (or until the stopping criteria was satisfied) with a minibatch size of 8. Stem networks were fine-tuned with a fixed, reduced learning rate of 0.00002 for 100K iterations. 3D patches of shape  $40 \times 64 \times 64$  (ZYX axes ordering) were used. Patches were augmented with random rotations, flips and elastic deformations. Gaussian noise was added to the input before passing through  $f(\cdot)$  and  $g(\cdot)$  networks.

**Electron microscopy datasets.** 2D U-Net architecture for the VNC and MitoEM datasets is shown in Table 8. The source VNC network was trained for up to 100K iterations with a minibatch size of 4. MitoEM networks were fine-tuned with a fixed, reduced learning rate of 0.00002 for 100K iterations. 2D patches of shape  $448 \times 448$  were used. Patches were augmented with random rotations, flips and

1-channel 3D patch $x \in \mathbb{R}^{K \times M \times M \times 1}$
ConvBlockGN, 64, MaxPool $2 \times 2$
ConvBlockGN, 128, MaxPool $2 \times 2$
ConvBlockGN, 256, MaxPool $2 \times 2$
ConvBlockGN, 512, Upsample $2 \times 2$
Concat, 256 + 512
ConvBlockGN, 256, Upsample $2 \times 2$
Concat, 128 + 256
ConvBlockGN, 128, Upsample $2 \times 2$
Concat, 64 + 128
ConvBlockGN, 64, conv $1 \times 1$ , $d = 16$

Table 7. U-Net architecture for Ovules and Stem datasets,  $K = 40$ ,  $M = 64$ . All convolutions and max pooling operations are 3D.

1-channel image $x \in \mathbb{R}^{M \times M \times 1}$
ConvBlockGN, 16, MaxPool $2 \times 2$
ConvBlockGN, 32, MaxPool $2 \times 2$
ConvBlockGN, 64, MaxPool $2 \times 2$
ConvBlockGN, 128, MaxPool $2 \times 2$
ConvBlockGN, 256, MaxPool $2 \times 2$
ConvBlockGN, 512, MaxPool $2 \times 2$
ConvBlockGN, 1024, Upsample $2 \times 2$
Concat, 512 + 1024
ConvBlockGN, 512, Upsample $2 \times 2$
Concat, 256 + 512
ConvBlockGN, 256, Upsample $2 \times 2$
Concat, 128 + 256
ConvBlockGN, 128, Upsample $2 \times 2$
Concat, 64 + 128
ConvBlockGN, 64, Upsample $2 \times 2$
Concat, 32 + 64
ConvBlockGN, 32, Upsample $2 \times 2$
Concat, 16 + 32
ConvBlockGN, 16, conv $1 \times 1$ , $d = 16$

Table 8. U-Net architecture for VNC and MitoEM datasets,  $M = 448$ .

elastic deformations. Gaussian noise was added to the input before passing through  $f(\cdot)$  and  $g(\cdot)$  networks.

**Adversarial training.** As described in Section 3.4 we can train the embedding network using an adversarial approach, where an additional discriminator distinguishes the object masks coming either from our differentiable instance selection method or from the ground truth. In each discriminator’s training iteration we stack individual object masks (either ”soft” of ground truth) across the batch dimension and pass it to the discriminator. We found this approach to be more effective than combining the masks and essen-

tially discriminating between the ground truth foreground mask and predicted foreground mask (in the labeled region). We hypothesise that this forces the discriminator to correct discrepancies between the ground truth and ”soft” object masks.

For adversarial training we use Wasserstein GAN with gradient penalty (WGAN-GP) [19] objective function given by:

$$V_D(G, D) = \mathbb{E}_{\tilde{\mathbf{x}} \sim \mathbb{P}_g} [D(\tilde{\mathbf{x}})] - \mathbb{E}_{\mathbf{x} \sim \mathbb{P}_r} [D(\mathbf{x})] + \lambda \mathbb{E}_{\tilde{\mathbf{x}} \sim \mathbb{P}_{\tilde{\mathbf{x}}}} [(\|\nabla_{\tilde{\mathbf{x}}} D(\tilde{\mathbf{x}})\| - 1)^2] \quad (11)$$

$$L_{wgan} = V_G(G, D) = -\mathbb{E}_{\tilde{\mathbf{x}} \sim \mathbb{P}_g} [D(\tilde{\mathbf{x}})] \quad (12)$$

for the critic and the embedding network (generator) respectively.  $\mathbb{P}_r$  is the distribution of ground truth mask,  $\mathbb{P}_g$  is the distribution of predicted ”soft” masks and  $\mathbb{P}_{\tilde{\mathbf{x}}}$  is the sampling distribution. Table 9 shows the architecture of the critic used in the Ovules dataset experiments. Our final objective for the embedding network is given by:  $L_{SO} + \zeta L_{wgan}$  or  $L_{SO0} + \zeta L_{wgan}$  depending on whether full or sparse supervision is used. Training of the embedding network and the critic is done using the Adam optimizer with  $\beta_1 = 0.5$ ,  $\beta_2 = 0.9$  and initial learning rate of 0.0001 for both networks. We use  $n_{critic} = 5$  iterations per each iteration of the embedding network. We use  $\lambda = 10$  (GP weight) and  $\zeta = 0.1$  ( $L_{wgan}$  weight) in our experiments. In order to prevent uninformative gradients from the critic at the beginning of the training process,  $L_{wgan}$  is enabled after the warm-up period of 50K iterations.

1-channel image $x \in [0, 1]^{K \times M \times M \times 1}$
ConvBlock, 64, MaxPool $2 \times 2$
ConvBlock, 128, MaxPool $2 \times 2$
ConvBlock, 256, MaxPool $2 \times 2$
ConvBlock, 512, Upsample $2 \times 2$
dense layer, 1

Table 9. WGAN-GP critic architecture used in the adversarial setting on Ovules dataset,  $K = 40$ ,  $M = 64$ . All convolutions and max pooling operations are 3D. No batch or group normalization was used. ReLU was replaced by leaky ReLU activation function with  $\alpha = 10^{-2}$ .

## A.2. Ablation: loss functions

Table 10 presents segmentation and counting scores (CVPPP test set) with different loss variants. HDBSCAN with  $min\_size = 200$  and no foreground mask was used for clustering the network outputs in all cases.

In the bottom part of the table we report the ablation of the additional push term  $L_{U\_push}$  used in the semi-supervised setting. Training without the ”push” term

worsen the segmentation and counting scores in all experiments. E.g. in the sparse regime of 10% of the ground truth object the average difference in counting for network trained without  $L_{U\_push}$  deteriorated significantly. For completeness we also include the effect of removing the embedding consistency term  $L_{U\_con}$  already presented in the Section 4.3. We can see that the consistency term  $L_{U\_con}$  has stronger impact on the segmentation performance than the unlabeled "push" term  $L_{U\_push}$ .

Anchor selection described in Algorithm 1 (row 1) is compared with random choosing random anchors from ground truth objects (row 2) and selecting the mean object anchors (row 3). We see that both mean and random anchor sampling results in comparable segmentation metric (SBD), but mean anchors provide a better counting score ( $|DiC|$ ). Using anchor sampling (Algorithm 1) during training match the counting score of mean anchors, but also results in better segmentation score after HDBSCAN clustering.

We also explored the impact of the adversarial loss ( $L_{wgan}$ ) applied on the object level (row 4), but it did not lead to improved performance over the  $L_{SO}$  loss on the CVPPP dataset (see results on the Ovules dataset in Section 4.3 for comparison).

Loss function	SBD	$ DiC $
$L_{SO}$ w/ anchor sampling	0.886	1.3
$L_{SO}$ w/ random anchors	0.870	1.5
$L_{SO}$ w/ mean anchors	0.868	1.2
$L_{SO} + L_{wgan}$	0.864	1.8
@0.1	$0.788 \pm 0.017$	$5.4 \pm 0.3$
@0.1 w/o $L_{U\_push}$	$0.734 \pm 0.042$	$8.5 \pm 0.4$
@0.1 w/o $L_{U\_con}$	$0.720 \pm 0.037$	$6.3 \pm 0.1$
@0.4	$0.824 \pm 0.003$	$3.2 \pm 0.5$
@0.4 w/o $L_{U\_push}$	$0.779 \pm 0.045$	$3.0 \pm 0.7$
@0.4 w/o $L_{U\_con}$	$0.738 \pm 0.019$	$2.1 \pm 0.1$
@0.8	$0.828 \pm 0.010$	$1.6 \pm 0.2$
@0.8 w/o $L_{U\_push}$	$0.797 \pm 0.014$	$1.9 \pm 0.4$
@0.8 w/o $L_{U\_con}$	$0.810 \pm 0.010$	$2.1 \pm 0.2$

Table 10. Ablation study of different loss variants. We report segmentation (SBD) and counting ( $|DiC|$ ) scores on the CVPPP test set. Ablation of the  $L_{U\_dist}$  term in the semi-supervised setting is reported for 10%, 40% and 80% of randomly selected ground truth objects. Mean  $\pm$  SD are reported across 3 random samplings of the ground truth objects.

### A.3. Comparison of clustering algorithms

Quantitative comparison of 3 different clustering algorithms: HDBSCAN, Mean-shift and Consistency Clustering (see Algorithm 2) are shown in Table 11. We report the segmentation metrics on the CVPPP and DSB2018 datasets. We used the embedding networks trained using SPOCO@0.4 (i.e. 40% of randomly selected ground truth

objects) for both datasets.

On the DSB2018 test set the consistency clustering scheme (Algorithm 2) significantly outperforms the mean-shift and HDBSCAN with  $min\_size = 140$  chosen on the validation set. However it still falls short of the performance of fully supervised SPOCO clustered on the predicted foreground mask (see Section 4.3).

On The CVPPP test set, the HDBSCAN shows the best performance, particularly when looking at the counting scores ( $|DiC|$ ). Consistency clustering results in better counting scores than mean shift, but it is unable to filter out all the spurious instances given by the mean shift.

Qualitative results on sample test images are illustrated in Figure 7. Failure to segment small instances in the crowded DSB images when using HDBSCAN with a fixed  $min\_size$  can be seen in the last two rows. Consistency clustering performs much better, but some objects are missing due to the aggressive instance filtering used by the algorithm.

Method (CVPPP)	SBD	$ DiC $
Mean-shift	$0.815 \pm 0.014$	$95.5 \pm 13.4$
HDBSCAN	$0.824 \pm 0.003$	$3.2 \pm 0.5$
Consistency clust.	$0.777 \pm 0.009$	$32.1 \pm 6.3$
Method (DSB2018)	AP@0.5	mAP
Mean-shift	$0.104 \pm 0.003$	$0.071 \pm 0.001$
HDBSCAN	$0.444 \pm 0.020$	$0.269 \pm 0.004$
Consistency clust.	$0.613 \pm 0.024$	$0.352 \pm 0.009$

Table 11. Comparison of clustering methods. Mean-shift with bandwidth  $\delta_v = 0.5$ , HDBSCAN with  $min\_size = 200$  (CVPPP) and  $min\_size = 140$  (DSB2018) and Consistency Clustering with  $IoU = 0.6$  were used. SBD,  $|DiC|$  are reported on the CVPPP and AP@0.5, mAP on the DSB2018 test sets. Embedding network trained with SPOCO@0.4 was used for inference. Mean  $\pm$  SD are reported across 3 random samplings of the ground truth objects.

## References

- [1] M. Arjovsky, S. Chintala, and L. Bottou. Wasserstein generative adversarial networks. volume 70 of *Proceedings of Machine Learning Research*, pages 214–223, International Convention Centre, Sydney, Australia, 06–11 Aug 2017. PMLR.
- [2] M. Bai and R. Urtasun. Deep watershed transform for instance segmentation. In *2017 IEEE Conference on Computer Vision and Pattern Recognition (CVPR)*, pages 2858–2866, 2017.
- [3] A. Bailoni, C. Pape, S. Wolf, A. Kreshuk, and F. A. Hamprecht. Proposal-free volumetric instance segmentation from latent single-instance masks. *arXiv preprint arXiv:2009.04998*, 2020.
- [4] T. Beier, C. Pape, N. Rahaman, T. Prange, S. Berg, D. D. Bock, A. Cardona, G. W. Knott, S. M. Plaza, L. K. Scheffer, et al. Multicut brings automated neurite segmentation

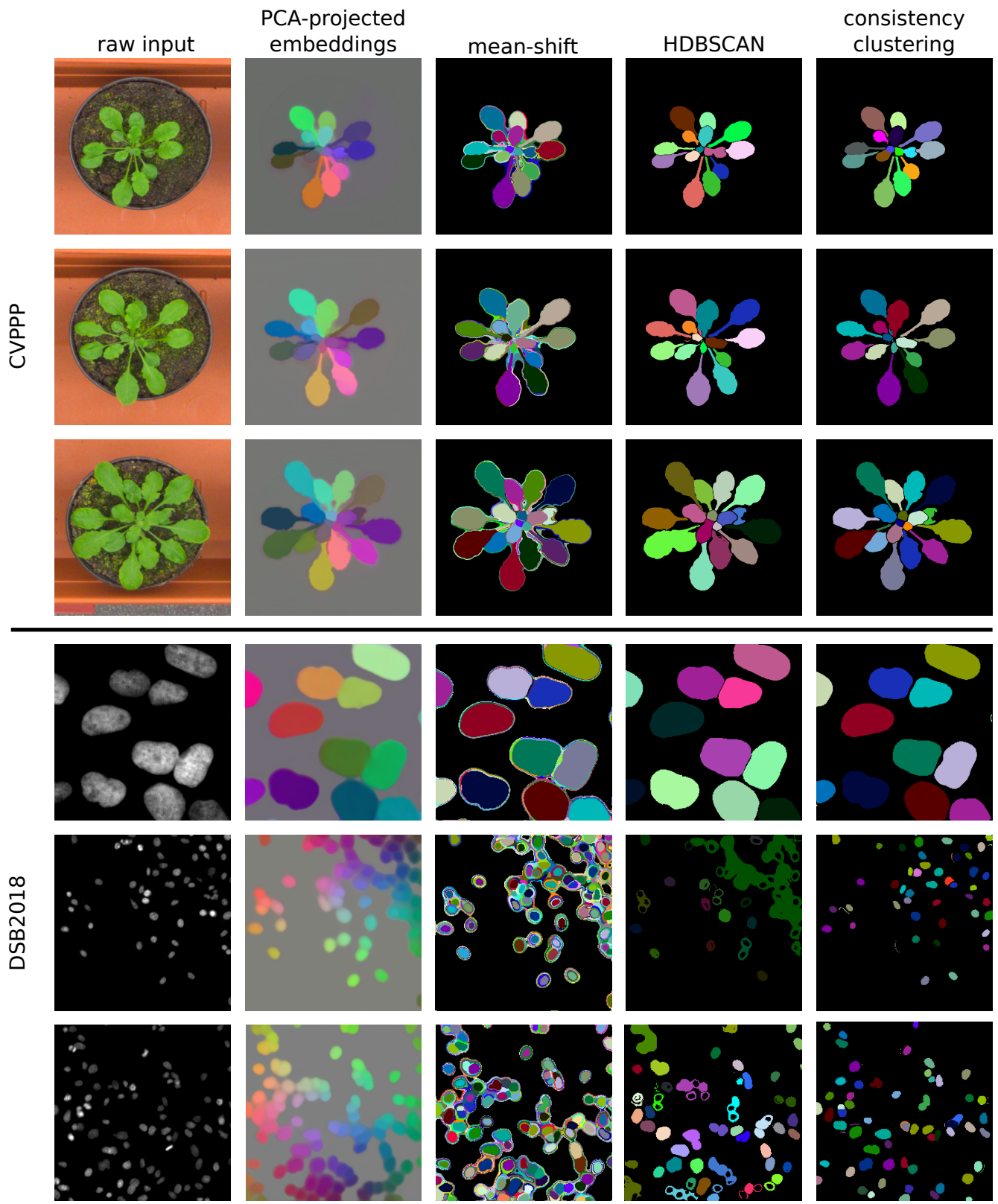


Figure 7. Qualitative comparison of different clustering schemes on the CVPPP and DSB2018 datasets. SPOCO@0.4 network was used for inference.

- closer to human performance. *Nature methods*, 14(2):101–102, 2017.
- [5] M. Bellver, A. Salvador, J. Torres, and X. Giro-i Nieto. Mask-guided sample selection for semi-supervised instance segmentation. *Multimedia Tools and Applications*, 79(35):25551–25569, 2020.
- [6] M. Bellver Bueno, A. Salvador Aguilera, J. Torres Viñals, and X. Giró Nieto. Budget-aware semi-supervised semantic and instance segmentation. In *The IEEE Conference on Computer Vision and Pattern Recognition (CVPR) Workshops, 2019*, pages 93–102, 2019.
- [7] B. D. Brabandere, D. Neven, and L. V. Gool. Semantic instance segmentation with a discriminative loss function, 2017.
- [8] R. J. Campello, D. Moulavi, and J. Sander. Density-based clustering based on hierarchical density estimates. In *Pacific-Asia conference on knowledge discovery and data mining*, pages 160–172. Springer, 2013.
- [9] L. Chen, W. Zhang, Y. Wu, M. Strauch, and D. Merhof. Semi-supervised instance segmentation with a learned shape prior. In *Interpretable and Annotation-Efficient Learning for Medical Image Computing*, pages 94–102. Springer, 2020.
- [10] X. Chen, H. Fan, R. Girshick, and K. He. Improved baselines with momentum contrastive learning, 2020.
- [11] B. Cheng, M. D. Collins, Y. Zhu, T. Liu, T. S. Huang, H. Adam, and L.-C. Chen. Panoptic-deeplab: A simple, strong, and fast baseline for bottom-up panoptic segmentation. In *Proceedings of the IEEE/CVF Conference on Computer Vision and Pattern Recognition*, pages 12475–12485, 2020.
- [12] Ö. Çiçek, A. Abdulkadir, S. S. Lienkamp, T. Brox, and O. Ronneberger. 3d u-net: Learning dense volumetric segmentation from sparse annotation. *CoRR*, abs/1606.06650, 2016.
- [13] D. Comaniciu and P. Meer. Mean shift: A robust approach toward feature space analysis. *IEEE Transactions on pattern analysis and machine intelligence*, 24(5):603–619, 2002.
- [14] CREMI. Creml. miccai challenge on circuit reconstruction from electron microscopy images, 2017. <https://cremi.org>, 2017.
- [15] J. Funke, F. D. Tschoop, W. Grisaitis, A. Sheridan, C. Singh, S. Saalfeld, and S. C. Turaga. A deep structured learning approach towards automating connectome reconstruction from 3d electron micrographs. *arXiv preprint arXiv:1709.02974*, 2017.
- [16] W. V. Gansbeke, S. Vandenhende, S. Georgoulis, and L. V. Gool. Unsupervised semantic segmentation by contrasting object mask proposals, 2021.
- [17] S. Gerhard, J. Funke, J. Martel, A. Cardona, and R. Fetter. Segmented anisotropic sstem dataset of neural tissue, 2013.
- [18] J.-B. Grill, F. Strub, F. Altché, C. Tallec, P. Richemond, E. Buchatskaya, C. Doersch, B. Avila Pires, Z. Guo, M. Gheshlaghi Azar, B. Piot, k. kavukcuoglu, R. Munos, and M. Valko. Bootstrap your own latent - a new approach to self-supervised learning. In H. Larochelle, M. Ranzato, R. Hadsell, M. F. Balcan, and H. Lin, editors, *Advances in Neural Information Processing Systems*, volume 33, pages 21271–21284. Curran Associates, Inc., 2020.
- [19] I. Gulrajani, F. Ahmed, M. Arjovsky, V. Dumoulin, and A. C. Courville. Improved training of wasserstein gans. In I. Guyon, U. V. Luxburg, S. Bengio, H. Wallach, R. Fergus, S. Vishwanathan, and R. Garnett, editors, *Advances in Neural Information Processing Systems*, volume 30. Curran Associates, Inc., 2017.
- [20] K. He, H. Fan, Y. Wu, S. Xie, and R. Girshick. Momentum contrast for unsupervised visual representation learning. In *Proceedings of the IEEE/CVF Conference on Computer Vision and Pattern Recognition (CVPR)*, June 2020.
- [21] K. He, G. Gkioxari, P. Dollár, and R. Girshick. Mask r-cnn. In *Proceedings of the IEEE international conference on computer vision*, pages 2961–2969, 2017.
- [22] P. Hirsch, L. Mais, and D. Kainmueller. Patchperpix for instance segmentation. *arXiv preprint arXiv:2001.07626*, 2020.
- [23] S. Ioffe and C. Szegedy. Batch normalization: Accelerating deep network training by reducing internal covariate shift. In F. Bach and D. Blei, editors, *Proceedings of the 32nd International Conference on Machine Learning*, volume 37 of *Proceedings of Machine Learning Research*, pages 448–456, Lille, France, 07–09 Jul 2015. PMLR.
- [24] Kaggle. 2018 data science bowl. <https://www.kaggle.com/c/data-science-bowl-2018>, 2018.
- [25] A. Khoreva, R. Benenson, J. Hosang, M. Hein, and B. Schiele. Simple does it: Weakly supervised instance and semantic segmentation. In *Proceedings of the IEEE conference on computer vision and pattern recognition*, pages 876–885, 2017.
- [26] D. P. Kingma and J. Ba. Adam: A method for stochastic optimization. In Y. Bengio and Y. LeCun, editors, *3rd International Conference on Learning Representations, ICLR 2015, San Diego, CA, USA, May 7-9, 2015, Conference Track Proceedings*, 2015.
- [27] V. Kulikov and V. Lempitsky. Instance segmentation of biological images using harmonic embeddings, 2020.
- [28] K. Lee, J. Zung, P. Li, V. Jain, and H. S. Seung. Superhuman accuracy on the snemi3d connectomics challenge. *arXiv preprint arXiv:1706.00120*, 2017.
- [29] Q. Li, A. Arnab, and P. H. Torr. Weakly-and semi-supervised panoptic segmentation. In *Proceedings of the European conference on computer vision (ECCV)*, pages 102–118, 2018.
- [30] R. Liu, J. Lehman, P. Molino, F. P. Such, E. Frank, A. Sergeev, and J. Yosinski. An intriguing failing of convolutional neural networks and the coordconv solution. In *Advances in Neural Information Processing Systems*, pages 9605–9616, 2018.
- [31] P. Luc, C. Couprie, S. Chintala, and J. Verbeek. Semantic segmentation using adversarial networks, 2016.
- [32] F. Milletari, N. Navab, and S.-A. Ahmadi. V-net: Fully convolutional neural networks for volumetric medical image segmentation, 2016.
- [33] M. Minervini, A. Fischbach, H. Scharr, and S. A. Tsafaris. Finely-grained annotated datasets for image-based plant phenotyping. *Pattern Recognition Letters*, pages –, 2015.
- [34] D. Neven, B. D. Brabandere, M. Proesmans, and L. V. Gool. Instance segmentation by jointly optimizing spatial

- embeddings and clustering bandwidth. In *Proceedings of the IEEE/CVF Conference on Computer Vision and Pattern Recognition (CVPR)*, June 2019.
- [35] K. Nishimura, R. Bise, et al. Weakly supervised cell instance segmentation by propagating from detection response. In *International Conference on Medical Image Computing and Computer-Assisted Intervention*, pages 649–657. Springer, 2019.
- [36] C. Pape, A. Matskevych, A. Wolny, J. Hennies, G. Mizzon, M. Louveaux, J. Musser, A. Maizel, D. Arendt, and A. Kreshuk. Leveraging domain knowledge to improve microscopy image segmentation with lifted multicuts. *Frontiers in Computer Science*, 1:6, 2019.
- [37] C. Payer, D. Štern, M. Feiner, H. Bischof, and M. Urschler. Segmenting and tracking cell instances with cosine embeddings and recurrent hourglass networks. *Medical Image Analysis*, 57:106–119, oct 2019.
- [38] M. Ren and R. S. Zemel. End-to-end instance segmentation with recurrent attention, 2017.
- [39] O. Ronneberger, P. Fischer, and T. Brox. U-net: Convolutional networks for biomedical image segmentation. In *International Conference on Medical image computing and computer-assisted intervention*, pages 234–241. Springer, 2015.
- [40] U. Schmidt, M. Weigert, C. Broaddus, and G. Myers. Cell detection with star-convex polygons. In *Medical Image Computing and Computer Assisted Intervention - MICCAI 2018 - 21st International Conference, Granada, Spain, September 16-20, 2018, Proceedings, Part II*, pages 265–273, 2018.
- [41] K. Sofiiuk, O. Barinova, and A. Konushin. Adaptis: Adaptive instance selection network. In *Proceedings of the IEEE/CVF International Conference on Computer Vision*, pages 7355–7363, 2019.
- [42] C. Song, Y. Huang, W. Ouyang, and L. Wang. Box-driven class-wise region masking and filling rate guided loss for weakly supervised semantic segmentation. In *Proceedings of the IEEE/CVF Conference on Computer Vision and Pattern Recognition*, pages 3136–3145, 2019.
- [43] D. Wei, Z. Lin, D. Barranco, N. Wendt, X. Liu, W. Yin, X. Huang, A. Gupta, W. Jang, X. Wang, I. Arganda-Carreras, J. Lichtman, and H. Pfister. Mitoem dataset: Large-scale 3d mitochondria instance segmentation from em images. In *International Conference on Medical Image Computing and Computer Assisted Intervention*, 2020.
- [44] L. Willis, Y. Refahi, R. Wightman, B. Landrein, J. Teles, K. C. Huang, E. M. Meyerowitz, and H. Jönsson. Cell size and growth regulation in the arabidopsis thaliana apical stem cell niche. *Proceedings of the National Academy of Sciences*, 113(51):E8238–E8246, 2016.
- [45] A. Wolny, L. Cerrone, A. Vijayan, R. Tofanelli, A. V. Barro, M. Louveaux, C. Wenzl, S. Strauss, D. Wilson-Sánchez, R. Lymbouridou, S. S. Steigleder, C. Pape, A. Bailoni, S. Duran-Nebreda, G. W. Bassel, J. U. Lohmann, M. Tsiantis, F. A. Hamprecht, K. Schneitz, A. Maizel, and A. Kreshuk. Accurate and versatile 3d segmentation of plant tissues at cellular resolution. *eLife*, 9:e57613, jul 2020.
- [46] Y. Wu and K. He. Group normalization. In *Proceedings of the European Conference on Computer Vision (ECCV)*, September 2018.